Chapter 2
Elastic Light Scattering of Biopolymer/Gold Nanoparticles Fractal Aggregates

Glauco R. Souza and J. Houston Miller

1 Introduction

From the interface of biotechnology and nanotechnology are emerging innovative analytical tools for the detection and characterization of nucleic acids, proteins, and protein interactions. This chapter addresses the development and application of a technique that combines angle-dependent light scattering (ADLS), fractal dimension analysis (FD), and gold nanoparticle assembly to detect and characterize nucleic acids and proteins. We will show that specific DNA or protein interactions trigger the assembly of Au-biopolymer fractal aggregates. The angle-resolved light-scattering signal from these aggregates can be used to determine their fractal dimension which is found to be sensitive to concentration, size, shape, and physical properties of both the biopolymers and the nanoparticles forming the aggregates [1, 2].

Researchers in the fields of material and combustion sciences have used ADLS and fractal dimension analysis (ADLS/FD) to study the structure and the formation of colloidal and soot particle aggregates (see Table 2.1) [1, 5, 27, 34–48]. Fractals are self-similar or scale-invariant objects [49, 50]. Regardless of the magnification of an object relative to a given variable, such as length, area, volume, or radius of gyration, the structure of a fractal remains statistically unchanged [48]. The Au colloid aggregate shown in Fig. 2.1 is an example of a fractal object, where the structure of small regions of the aggregate resembles the overall aggregate structure [51].

In this chapter, we will review work performed to analyze elastic light scattering from fractal aggregates and describe some of the work performed in our laboratory to extend this technique to the detection and characterization of biopolymers.

G.R. Souza
Nano3D Biosciences Inc., 7000 Fannin Street, Suite 2140, Houston, TX 77030, USA

J.H. Miller (✉)
Department of Chemistry, The George Washington University, Washington, DC 20052, USA

C.D. Geddes (ed.), *Reviews in Plasmonics 2010*, Reviews in Plasmonics,
DOI 10.1007/978-1-4614-0884-0_2, © Springer Science+Business Media, LLC 2012

Table 2.1 Partial summary of literature on fractal agglomerate and scattering phenomena

Sample type	Technique	Ref.
Colloid	Theoretical calculation	[3]
Latex	Optical microscopy	[4]
Hematite	Light scattering	[5]
Latex	Light scattering	[6]
Au–DNA	Light scattering	[1]
Au colloid	TEM	[7]
Au–protein	Light scattering	[1]
Vaporized metal	Transmission electron microscope (TEM)	[8]
Silica	Light and X-ray scattering	[9]
Au colloid	TEM	[10]
Au colloid	Dynamic light scattering and theoretical calculations	[11]
Au colloid	Dynamic Light scattering, TEM and light scattering	[12]
Silica aerogel	Small-angle X-ray scattering	[13]
Protein-surfactant (BSA-LDS)	Small angle neutron scattering (SANS)	[14]
Silica	Static light scattering	[15]
Au colloid	X-ray scattering	[16]
Silica	SANS	[17]
Silica vapor	Light scattering	[18]
Au colloid	Dynamic light scattering	[19]
Silica	Light scattering	[20]
Au colloid	Dynamic light scattering	[21]
Hematite	Dynamic light scattering	[22]
Au colloid	Dynamic light scattering	[21]
Au colloid	Light scattering and TEM	[23]
Polystyrene latex	Light scattering	[24]
Silica and carbon black	X-ray scattering and SANS	[25]
Silica aerogels	SANS	[26]
Soot aerogels	Light scattering	[27]
Polystyrene	Light scattering	[28]
Soot aerogel	TEM	[29]
Polystyrene latex	Light scattering	[30]
Polystyrene	Light scattering	[31]
Haematite	X-ray scattering	[32]
Ag colloid	TEM	[33]

1.1 Simple Light Scattering Theories: Rayleigh Through Mie

Light scattering is a natural phenomenon that is part of our everyday lives. Rarely is light observed directly from its original source but rather is a result of scattered light [52]. For example, blue skies and red sunsets occur because sunlight is scattered by molecules and particles in the atmosphere, respectively [53]. The observation of blue skies at midday and red skies at sunrise and sunset provide clues about the dependence of scattering signal on not only the size of the particles, but also the angular dependence of the scattered light from the source to the scatterer to the observer [54].

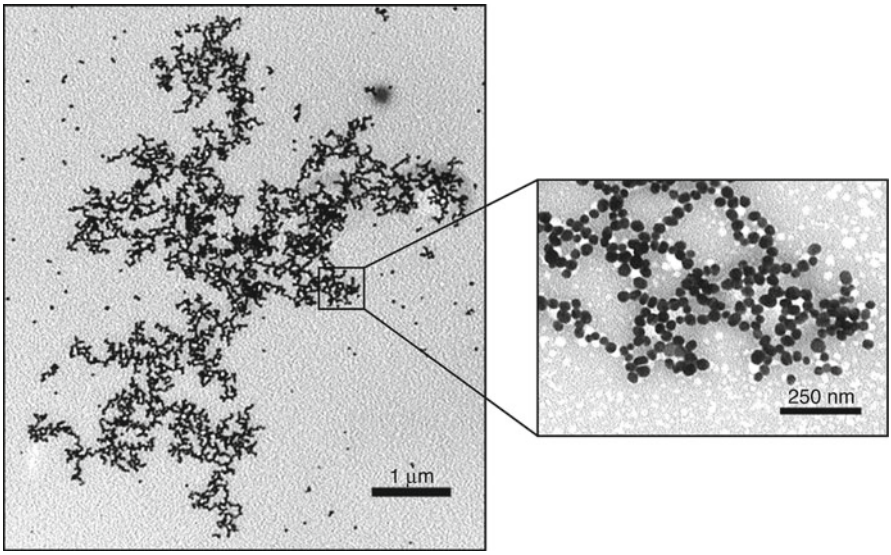

Fig. 2.1 Scanning electron microscope image of Au colloid fractal

It is important to distinguish the meaning of the terms "absorption" and "extinction." The measurement of light extinction (such as that provided in a simple UV/Vis absorption spectrophotometer) reports the sum of scattering and absorption, since both phenomenon attenuate the intensity of a light beam traveling across a medium [55–57]. In this chapter, both phenomenon might occur in the same sample. For example, the observation of surface plasmon absorption in suspensions of gold nanoparticles is an absorption phenomenon as surface plasmon electrons are being excited from one state to another [55]. In the same sample, aggregation of the nanoparticles leads to extinction at both shorter and longer wavelengths that is attributable to scattering from the aggregates particles.

Light scattering can be differentiated as elastic or inelastic light scattering. Inelastic light scattering occurs when the scattered light has a wavelength shift relative to the wavelength of the incident light. This frequency shift can be either higher or lower, depending on if there is a loss or gain of energy of the scattering substance. Examples of inelastic light scattering are Raman and dynamic light scattering. In this chapter, we refer almost exclusively to elastic scattering, where the incident and scattered wave have the same wavelength. However, we will conclude by showing how inelastic scattering might be used to provide complementary information about aggregation of systems of gold nanoparticles induced by biopolymer interactions.

The foundation of light-scattering theory was initially developed near the end of the nineteenth century and in first half of the twentieth century by Rayleigh, Mie, Smoluchowski, Einstein, and Debye motivated in part by the experimental work of Tyndall [58]. In addition to providing an explanation for scattering in the atmosphere, Rayleigh also studied scattering from spheres of arbitrary sizes, where phase

relations between the light scattered from different regions of the same particles were regarded as localized, independent, and induced dipoles. In the early 1900s, Debye further developed scattering theory for larger and nonspherical particles.

Matter consists of electrically charged nuclei and electrons that can interact with an oscillating electromagnetic field, e.g., light, and either absorb or scatter light. In either case, there is attenuation in the light intensity, which is described by the exponential decay of the light intensity as it passes through a medium [52, 55, 56, 59]:

$$I = I_0 \mathrm{e}^{-kx} \tag{2.1}$$

where I is the intensity of the light transmitted after traveling a distance x across the medium. k changes in definition (and symbol) for different forms of extinction. For molecular absorption, it is the absorption coefficient.[1] For scattering, the extinction coefficient is often given the symbol τ, the turbidity of the medium. In this context, it is related to the number density of particles (n) and their individual extinction cross-section (σ_{ext}),

$$\tau = n \times \sigma_{\mathrm{ext}}. \tag{2.2}$$

As noted above, extinction is due to both scattering, which removes light from the incident path by reemitting light in all directions, and absorption, which converts the light into other forms of energy (such as heat). Mathematically,

$$\sigma_{\mathrm{ext}} = \sigma_{\mathrm{abs}} + \sigma_{\mathrm{scatt}}, \tag{2.3}$$

where σ_{abs} and σ_{scatt} are the absorption and scattering cross sections, respectively. This relationship is valid for all particle and molecular systems [56].

As noted, since the late nineteenth century, the relative size of the scatterer and the wavelength of light are critical dependencies of the scattering intensity. For spheres, it is convenient to define the size parameter, α, as a relative measure of the magnitude of the particle radius (a) and the wavelength of light (λ).

$$\alpha = \frac{2\pi a}{\lambda}. \tag{2.4}$$

Rayleigh scattering is the best and simplest mathematical description for the scattering from particles that are small, relative to the wavelength of light. Generally, for Rayleigh scattering we require [52, 54–57, 60]:

$$\alpha << 1 \quad \text{and} \quad m\alpha << 1, \tag{2.5}$$

[1] Chemists remember the extinction coefficient as the product of the molar extinction coefficient and the molar concentration. Gas phase spectroscopists cast this as the product of the gas density, the absorbing species' line strength, and a line shape factor that accounts for how the line is broadened from molecular collisions and molecular motion.

where m is the relative refractive index of the scattering particle. A quantity that is often used to describe a scattering object is its differential scattering cross section,

$$\frac{d\sigma}{d\Omega} = \frac{16\pi^4 a^6}{\lambda^4}\left|\frac{m^2-1}{m^2+2}\right|^2 \tag{2.6}$$

which is related to the power scattered (P_{scat}) per unit solid angle (Ω) through [55, 56]:

$$\frac{P_{scat}}{\Omega} = \frac{d\sigma}{d\Omega} I_0, \tag{2.7}$$

where the intensity of incident radiation is I_0.

If the differential scattering cross section is integrated over all space, the total scattering cross section is given by

$$\sigma_{scatt} = \frac{8\pi}{3}\frac{16\pi^4 a^6}{\lambda^4}\left|\frac{m^2-1}{m^2+2}\right|^2. \tag{2.8}$$

Thus, if the quantity $|(m^2-1)/(m^2+2)|^2$ is weakly dependent on λ, the scattered intensity shows the familiar λ^{-4} dependence.

If the incident light and the scattered light have the same polarization (referred to as "parallel" scattering), the angular distribution of the scattered light depends on the polarization of the incident light. Specifically,

$$I_\perp = \frac{1}{r^2}\frac{16\pi^4 a^6}{\lambda^4}\left|\frac{m^2-1}{m^2+2}\right|^2 I_0, \tag{2.9}$$

$$I_\parallel = \frac{1}{r^2}\frac{16\pi^4 a^6}{\lambda^4}\left|\frac{m^2-1}{m^2+2}\right|^2 \cos^2\theta I_0, \tag{2.10}$$

$$I = \frac{1}{2}\left(I_\perp + I_\parallel\right) = \frac{1}{r^2}\frac{16\pi^4 a^6}{\lambda^4}\left|\frac{m^2-1}{m^2+2}\right|^2 \left(1+\cos^2\theta\right) I_0, \tag{2.11}$$

where $I_\perp$, $I_\parallel$ and I are the intensities of vertically polarized light, horizontally polarized light, and unpolarized light, respectively [55].

As noted by Sorensen [56], three features of Rayleigh scattering can be highlighted:

- The scattering of vertically polarized light is independent of θ and it is isotropic in the scattering plane
- I is a function of λ^{-4}, which implies that short wavelength light scatters more efficiently
- There is large size dependence for the scattered intensity through the a^6 term (proportional to the square of the particle volume). This third feature is often referred to as the Tyndall effect [56, 60]

As seen in (2.3), particles and molecules both scatter and absorb light. For molecules, absorption is described in terms of the interaction of two molecular wavefunctions through the dipole moment operator. For particles, the Rayleigh absorption cross-section is given by

$$\sigma_{\text{abs}} = \frac{8\pi^2 a^3}{\lambda} \text{Im}\left(\pi \frac{m^2 - 1}{m^2 + 2} \right). \tag{2.12}$$

If the relative refractive index is real, there is no absorption [52, 55–57].

Because σ_{abs} and σ_{scatt} have different wavelength, λ, and size, a, dependencies and the scattering cross section depends on both polarization and angle, it is clear that significant information about a particle's morphology is available from interrogation of the scattering signal. While these relationships have been shown explicitly for Rayleigh scatterers, we will show below that similar relationships hold for other scattering regimes [56].

Rayleigh scattering theory is derived with the assumption that the phase of the incident electromagnetic wave does not change across the particle. This requirement [$\alpha << 1$ in (2.5)] is relaxed in the Rayleigh–Gans–Debye (RGD) scattering theory [52, 55–57, 60] if

$$|m - 1| \ll 1, \tag{2.13}$$

$$2\alpha |m - 1| \ll 1. \tag{2.14}$$

The RGD scattering cross section for perpendicular detection of light [56], is

$$\frac{d\sigma}{d\Omega_{\text{RGD}}} = \frac{d\sigma}{d\Omega_{\text{R}}} \left[\frac{9}{u^6} \left(\sin(u) - u \cdot \cos(u) \right)^2 \right], \tag{2.15}$$

where

$$u = qa, \tag{2.16}$$

and

$$q = \frac{4\pi}{\lambda} \sin\left(\frac{\theta}{2} \right). \tag{2.17}$$

q is the scattering wave vector which will be further described below.

Two important characteristics of RGD scattering are [56]:

- For $\theta = 0$, the cross-section reduces to the Rayleigh cross-section.
- In contrast to Rayleigh scattering, the scattering intensity is larger in the forward direction, and this anisotropy increases with increasing particle size. This increase in anisotropy with particle size allows us to use a simple analysis method, the dissymmetry ratio [54, 55, 60], to detect changes in the size of an

aggregate or coalescing particles. Here we calculate the ratio of the intensity of forward scattering to the intensity of back scattering. Larger ratios indicate a larger size for the scattering particle.

Rayleigh and RGD scattering theories represent rigorous treatments of Maxwell's equations. For larger particles, where the approximations used to solve Maxwell's equations for a small particle are not valid, more complex dependencies on angular scattering intensity are observed. For example, Mie scattering theory is often applied to characterize scattering in biological systems [61]. However, Mie scattering should only be applied to systems of spherical symmetry. Even then, the angular distribution of scattering intensity makes it difficult to extract physical insight, particularly when the size distribution is polydispersed.

1.2 Fractal Structures and Scattering

The definition of fractals was first introduced in 1975 by Mandelbrot's in his work [46] *Les Objets Fractals: forme, hazard et dimension* [50] to describe objects that are self-similar or scale-invariant [49, 50]. Regardless of the magnification of an object relative to a given variable, such as length, mass, area, volume, or radius of gyration, the structure of a fractal remains statistically unchanged [48]. Fractal structures and fractal events manifest themselves in many aspects of nature, such as in the distribution of celestial bodies, structure of snowflakes, organization of tree branches, and in the structure of proteins. Fractal events are often identified in phase transition, growth, and diffusion phenomena [48].

Because scattered waves from individual primary particles interfere with one another [62], "classical" light-scattering theories fail to describe the ADLS pattern from an aggregate of noncoalescing particles (Fig. 2.2). New theories have been developed that characterize scattering from these aggregates as a function of the fractal dimension [3, 9, 41, 46, 56, 63–76]. As will be shown below, under certain conditions, the ADLS signal $I(\theta)$ is related to the fractal dimension (D_f) of an aggregate through [38, 46, 56, 63] .

$$I(\theta) \propto q(\theta)^{-Df}. \tag{2.18}$$

Thus a simple data-processing step can be used to quantify this important physical parameter of the scattering system. In the biological systems in focus here, this parameter can be related to the chemistry that forms the particle and is thus of analytical value.

Scattering models based on RGD theory are often used to describe the scattering signal from fractal aggregates [3, 46, 56, 67, 77, 78]. The assumption implicit in this use is that multiple scattering is negligible, and that the individual scatterers are small enough to behave like Rayleigh scatterers. Although the assumption that the

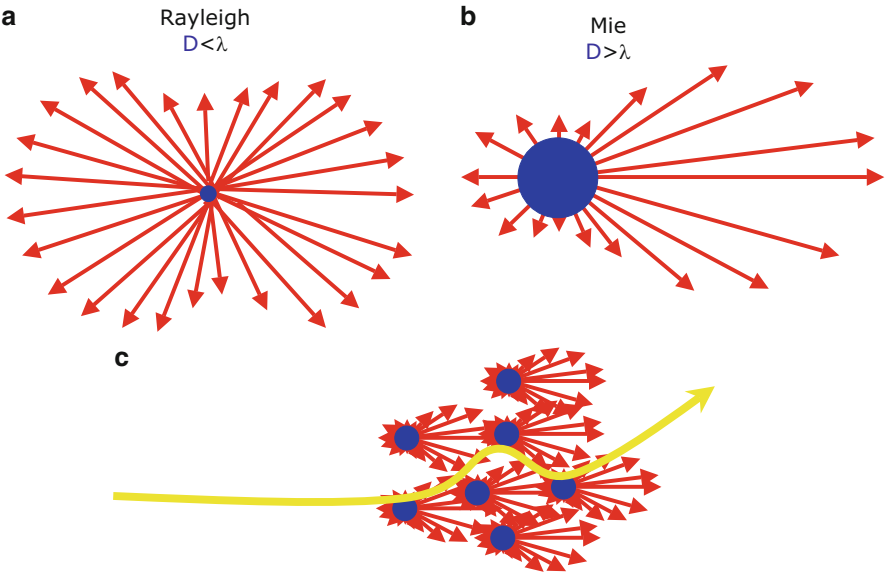

Fig. 2.2 Representation of parallel scattering patterns for (**a**) Rayleigh, (**b**) Mie, and (**c**) RGD-FA particles

individual particles scatter independently is not always accurate, RGD theory provides a reliable approximation when the following conditions exist [3, 46]:

$$|m-1| \ll 1 \quad \text{and} \quad \frac{2\pi a}{\lambda}|m-1| \ll 1, \tag{2.19}$$

where, a is now the radius of the primary particles and m is the relative refractive index of the primary particles. Farias and coworkers [3] have shown that, within 10% accuracy, RGD theory can predict the scattering signal with more relaxed constraints:

$$|m-1| \leq 1 \quad \text{and} \quad \frac{2\pi a}{\lambda}|m-1| \leq 0.6. \tag{2.20}$$

This method is referred to as the RGD approximation for the optical cross-section of fractal aggregates, RGD-FA.

In addition to the fractal dimension, another important parameter often used to characterize morphology of fractal aggregates is the Radius of Gyration, R_g which describes how mass is distributed around an arbitrary rotation axis. In mechanics, it is the square root of the moment of inertia divided by mass. Thus, R_g is functionally

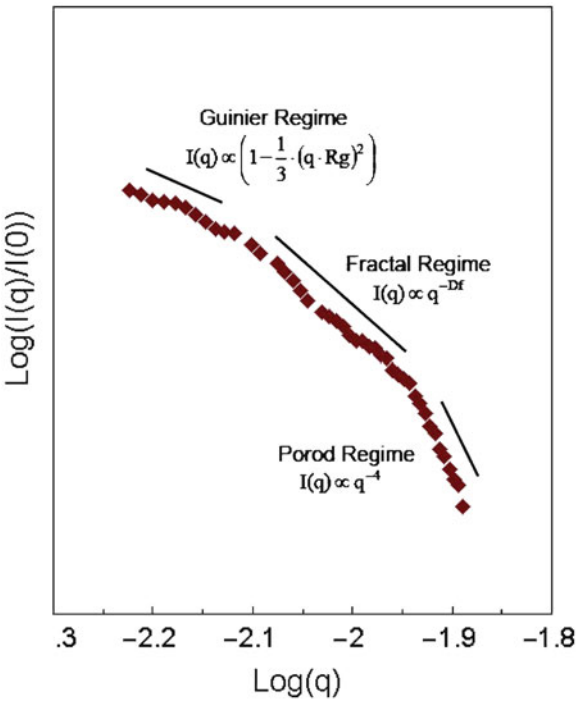

Fig. 2.3 Fractal dimension analysis of scattering signal from 100 nm Au aggregated with a protein showing aggregate light scattering regimes: Guinier, fractal and Porod regimes

a root mean square radius for the aggregate. Further, it is related to the number of primary particles in the aggregate and the fractal dimension through

$$N_{\mathrm{p}} = k_{\mathrm{p}} \left(\frac{R_{\mathrm{g}}}{a} \right)^{\mathrm{Df}}. \tag{2.21}$$

In practical terms, the inverse of q (which has units of length) is the size resolution limit of the scattering measurement. A scattering measurement is only sensitive to the structures of size greater than q^{-1}; thus, a scattering measurement is "blind" to structures smaller than q^{-1}. The scattering from a fractal aggregate can be separated into three regimes as a function of q: the fractal regime, the Guinier Regime and the Porod regime, as illustrated in Fig. 2.3. The scattering signal dependence as a function of q in the Guinier regime results from the overall size of the aggregate, where the size of the aggregates is smaller than the inverse of the wave vector ($q < 1/R_{\mathrm{g}}$). In the drop-off region at high values of q, q^{-1} is larger than the size of the individual particles (or $q > 1/a$). In this regime, referred to as the Porod regime, the scattering is attributed to dispersed particles. The intermediate regime is the fractal regime. Here, the scattering intensity is sensitive to the morphology and overall structure of the scattering aggregate, where q^{-1} is smaller than the R_{g} of the aggregate but larger than size of the individual particles making up the aggregate [56].

In most experiments, polydispersity and heterogeneity (for both the primary particle size distribution and that of the aggregates) always exist and the transition regions from one regime to the next are generally broader and less well defined than the conditions defined above [75, 76, 79]. Even so, the qualitative behavior predicted for light-scattering intensity as a function of angle (through q) is often observed. For example, Fig. 2.3 shows the scattering signal from gold-protein aggregates (see below), where the Guinier, fractal, and Porod regions are clearly evident.

To summarize, fractal aggregate-scattering theory predicts several diagnostic regimes in which the light scattering shows different dependencies on fundamental physical characteristics of the aggregate, notably the radius of gyration and the fractal dimension. Further, manipulation of the angular distribution data can be used to readily extract these quantities. In the Guinier regime, the scattering signal can be rewritten as

$$\frac{I(0)}{I(q)} \propto \frac{1}{3} q^2 R_g^{\ 2}. \tag{2.22}$$

Therefore a plot of $I(0)/I(q)$ vs. q^2, should yield a linear curve with slope of $\frac{1}{3} R_g^{\ 2}$. In the fractal regime, scattering signal is related to the fractal dimension through

$$I(q) \propto q(\theta)^{-\mathrm{Df}}. \tag{2.23}$$

Here the slope of a log–log plot of $I(q)$ vs. q gives the fractal dimension.

2 Experimental Considerations

Traditionally, light-scattering measurements have been performed either by collecting light at a single angle [80–84] or by placing a detector on a rotating stage and collecting the light as the stage rotates across different angles [27, 41, 74, 85]. Both detection schemes have limitations. The first offers fast detection, but, generally, single angle detection cannot be used to differentiate between multiple particle sizes without being coupled to a particle separation technique, such as gel filtration or chromatography [86–89]. The second scheme can provide good angle resolution and it can be used to differentiate between particles of various sizes without the need of a separation technique; however, this scheme is time-consuming because it is limited by the speed of the rotating stage and the detector integration time.

In our work, two apparatuses have been constructed. In the first, a rotating detection optics rail was used to resolve the angular intensity distribution. This can detect scattering angles ranging from 20° to 155° with angular resolution of approximately 6°. The second apparatus used a more elegant design, where an ellipsoidal mirror coupled to a CCD detector was used to detect and resolve the full scattering angle range in a single frame [90]. This apparatus provides fast detection, superior angular resolution, and wider scattering angle detection range compared to traditional light scattering

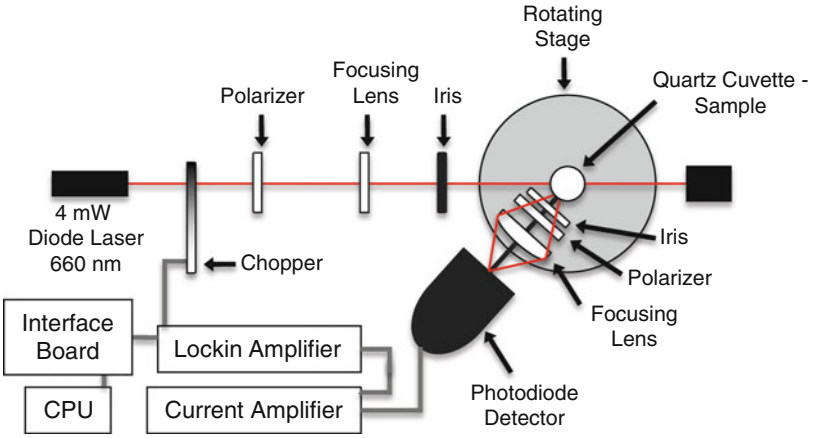

Fig. 2.4 Experimental arrangement used for collecting angle-resolved light scattering using a rotation detection optics arm

detection [54]. We found that the CCD-based apparatus could detect scattering signal in the range of 15–160° in a fraction of a second with angular resolution as low as 0.2°. Further details on these systems are provided below.

2.1 Rotation Stage Apparatus

The general schematic of the optical setup for the rotation stage apparatus is shown in Fig. 2.4. The light source was a 4 mW Fabry–Perot diode laser (equipped with a 3-Element Glass Lens, Edmund) with an output wavelength of 660 nm. The incident beam is modulated by a mechanical chopper (running at 1 KHz) that triggered a lock-in amplifier for phase-sensitive detection. The polarization of light can be selected by placing a polarizer before the 10-cm focal point focusing lens. The beam was focused into the center of a 1-cm diameter quartz-scattering cell. All light collection components are mounted on a manual rotation stage. The scattered light passes through a second polarizer that isolates the polarization of the scattered light, and then it is focused onto a silicon photodiode detector. An iris positioned in front of the detector provided approximately 6° angular resolution.

The scattering signal was collected as the detector arm rotated stepwise across the desired angles defined by the rotation stage and imaging iris. The photodiode signal is fed into a current amplifier with 1×10^6 gain. The amplified signal was sent to the lock-in amplifier for first harmonic detection. Custom LabView software on a Windows-based personal computer controlled the data collection and data analysis.

An inherent challenge for all light-scattering measurements is to reduce the background generated by stray light from reflection, diffraction, and scattering from optical components [91] and particulate matter. Stray light can result from imperfections

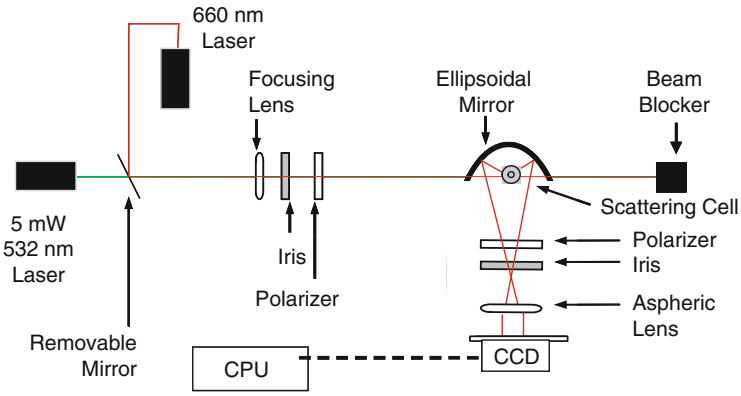

Fig. 2.5 Experimental arrangement used for collecting angle-resolved light scattering using the ellipsoidal mirror/CCD apparatus

in the glass wall of the scattering cell and from changes in the refractive index at the cell air/glass and glass/liquid interfaces as the laser beam enters/exits the scattering cell. In this apparatus, forward-scattered light from the walls of the cuvette compromised the measurements for scattering angles less than 20°. In order to minimize the impact of stray light, background subtraction in a suitable "blank" system can be used. In our measurements, we used either buffer solutions or pure water as a background that could be subtracted from the sample signal.

2.2 CCD-Based Apparatus

Figure 2.5 is a schematic diagram of the ellipsoidal mirror and CCD apparatus. The laser consists of either a 5 mW, 532-nm laser (a diode laser-pumped Nd:YVO_4 crystal coupled with KTP as a frequency doubler) or a 632 nm, 10 mW power Fabry–Perot laser. The laser used in a given experiment could be selected using a flip mirror. Either beam first goes through a polarizer and then it is focused into the center of a custom scattering cell through a 100 mm focal length lens. The scattering cell sits on a translation stage located approximately at one of the two focal points of an ellipsoidal mirror [90]. The ellipsoidal mirror is tilted approximately 35° downward relative to the scattering plane that minimized scattered light from reaching the detector.

The scattered light passed through a polarizer, which isolates the scattered light with the same polarization as the incident light, and then through an iris. Finally, a 1″ aspherical lens (with a focal length of 21 mm) focuses the scattered light onto the CCD array detector. The camera used had a 19.4 mm × 19.4 mm cooled CCD chip (1,024 × 1,024 pixels, EG&G PARC CCD detector model 1530-P-1024I). A mechanical shutter controls the light exposure of the CCD detector.

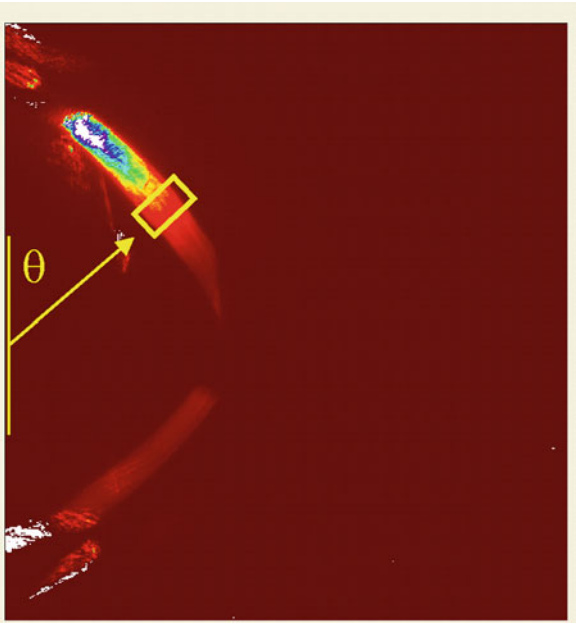

Fig. 2.6 CCD image illustrating angular distribution of scattering

The resulting CCD image is an arch, as shown in Fig. 2.6, from which a plot of scattered light intensity as a function of scattering angle can be extracted. In principle, the angular resolution is defined by the width of the of the CCD pixels (here, 19×19 μm^2/pixel). In contrast to the rotation stage apparatus, this optical configuration can detect a full scattering angle profile in a single shutter shot with an angle resolution of approximately 0.2° per pixel. Binning of adjacent pixels reduces this resolution but can increase experimental throughput and lower noise.

A computer controls data storage and data analysis. The HIDRIS image software provided with the CCD detector controls scattering data collection. Image files are further analyzed using custom software that converts the image files into a two-dimensional array, subtracts a background image of scattering, and extracts and plots the angular scattering intensity.

To calibrate the angular distribution of scattering intensity, a mixture of a fluorescent dye and 100 nm Au nanoparticles was placed in the sample holder. This solution provides an isotropic scattering signal. The fluorescent dye is Cy3, which emits at 558 nm with 530 nm excitation [92]. A slit mounted on a rotation stage could be used to mask a portion of the scattered intensity onto the detector. The two dimensional location of the resulting spot on the CCD image was then correlated to angle.

As already noted, an inherent challenge for all light scattering measurements is to reduce the background generated by changes in the refractive index as light travels through different media [91]. In this apparatus, the scattering cell used a outer jacket of toluene as an index matching medium between the two reservoirs [90] (Toluene's refractive index is 1.43 which is approximately the same as glass, 1.40 [55]).

2.3 Au Nanoparticles

The most common technique for the synthesis of Au nanoparticles is reduction of Au salts, often using sodium citrate as the reducing agent [93–98]. This method consists of dissolving auchloric acid trihydrated in high purity boiling water, and then reducing the Au salt with specific amounts of trisodium citrate. The concentration of Au salt relative to the concentration of sodium citrate determines the rate of nucleation, which, consequently, determines the final size of the Au nanoparticles. The reduction of Au ions by citrate is accompanied by change in color from the pale yellow of Au salt to dark red of metallic Au colloids. The high purity water is necessary to avoid unwanted Au nucleation induced by impurities. The width of the size distribution of the Au colloids prepared with this method is approximately 10% relative to the mean particle size. These nanoparticles are usually purified by centrifugation or dialyzes, depending on the size of the nanoparticle being synthesized.

3 Studies of DNA–Au Nanoparticle Aggregates

In this section, we will discuss an application of the angle resolve fractal aggregate scattering technique to DNA detection. In summary, thiol-modified oligonucleotides are covalently attached to gold nanoparticles (Au–DNA probe) which hybridize to a target single-strand oligonucleotide of complementary sequence (oligo-target) in a liquid sample, forming an aggregate network of DNA and Au nanoparticles. Conceptually, we anticipate that a greater concentration of the targets in solution will lead to more compact fractal aggregate structure as cross linking occurs (Fig. 2.7).

3.1 Chemistry and Chemical Methods

The Au–DNA probes consisted of 100 nm gold nanoparticles separately modified with either 3′ end or with 5′ end hexanethiol functionalized oligonucleotide. The concentration of the particles was determined by absorbance measurements at 564 nm using an extinction coefficient of $1.62 \times 10^{11}\ M^{-1}\,cm^{-1}$ [82]. The probes were prepared by mixing 9.0 pM of citrate stabilized 100 nm of gold nanoparticles with 5 nM of either 5′ or 3′ end hexanethiol modified oligonucleotide (respectively) without any salt added and by incubating this solution for 24 h at 4°C. The oligonucleotides sequences used were:

5′ *end*: $HS(CH_2)_6$–CCC–GCG–CCC–3′
3′ *end*: 5′–CCC–GCG–CCC–$(CH_2)_6SH$

The hybridization temperature (melting temperature) for these olgonucleotides was approximately 36°C. Au–DNA probes were purified by centrifugation ($14{,}000 \times g$ for 15 min), where the supernatant was discarded and the precipitate, Au–DNA probes, were resuspended in hybridization buffer.

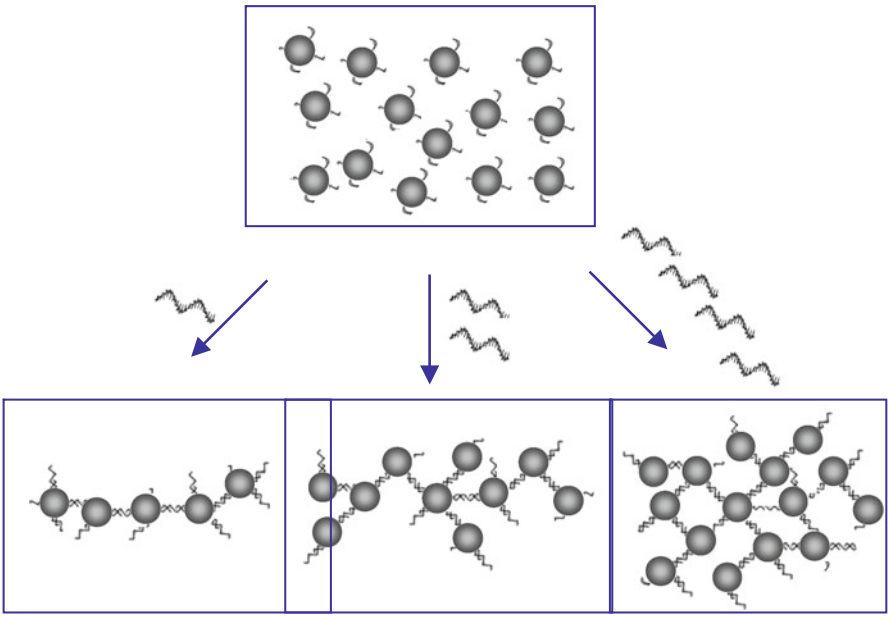

Fig. 2.7 Cartoon illustrating formation of Au–DNA fractal aggregate

The covalent linkage between the Au nanoparticle and the thiol-modified oligonucleotides was done through the thiol moiety and the Au nanoparticle. Although the chemistry of formation of self-assembled monolayers (SAM) of alkanethiols on Au surfaces and colloids has been studied extensively [99–102], there are still questions about the exact mechanism of attachment [103]. In one mechanism, which has been supported by experimental data and theoretical calculations [103–109], thiolate (RS^-) adsorbs on Au:

$$R-S-H+Au_n^0 \rightarrow R-S^-Au^+ \cdot Au_n^0 + \tfrac{1}{2}H_2$$

The thiolate–Au bond to gold surfaces is relatively strong, with a bond strength of approximately 40 kcal/mol [103, 104].

It has also been suggested by Whitesides and coworkers that the chemisorption process can occur with direct formation of a gold–sulfur bond, without the formation of thiolate [99].

$$R-S-H+Au_n^0 \rightarrow (\text{Au nanoparticle})-S-R + \tfrac{1}{2}H_2$$

Whitesides also suggested that Au^0 and Au^{+1} sites coexist, where Au^{+1} are occupied by citrate ions and thiols adsorb on Au^0 sites. The adsorbed citrate ions result from the original synthesis of Au nanoparticle. There is also experimental evidence

[103, 109], that at low coverage, both species, thiolates ($R–S^-$) and intact thiols (R–SH), coexist adsorbed on the Au surface.

Although there are different opinions on the exact mechanism of thiol chemisorption on gold, there is a consensus that chemisorption mechanism, of either intact thiols or thiolates, results in the formation of molecular hydrogen (H_2). The formation of H_2 is energetically necessary to justify the high stability of thiol SAM formation on gold surfaces [99, 100, 103, 104, 110]. The theoretical coverage of these monolayers on Au is approximately 0.77 nmol/cm^2 [99]. However, the extent of HS-DNA primer bound to the Au nanoparticle will be dependent on solution conditions, such as salt concentration and presence of organic solvents [111–115].

3.1.1 Hybridization Procedure

The oligo-targets consisted of synthesized oligonucleotides of either 21 or 30 bases in length where the 9-base sequence on the 3′ and 5′ ends are complementary to the sequences of the Au–DNA probes. The oligonucleotide sequences are:

21 *bases*: 5′–GGG–CGC–GGG–ATA–GGG–CGC–GGG–3′
30 *bases*: 5′–GGG–CGC–GGG–AAA–TAA–AAT–AAA–GGG–CGC–GGG–3′

Samples consisted of 0.1 pM of Au–DNA probe and oligo-target concentrations ranging from 0 to 2,500 nM. The hybridization procedure consisted of three heat and cool cycles where the Au–DNA samples were denatured at 70°C in a water bath for 10 min and then annealed in an ice bath for another 10 min. After the third cycle, the samples were incubated for 24 h at 4°C. Each sample was removed from 4°C just before ADLS measurement; 100 μL extracted and then mixed with 900 μL of hybridization buffer.

All experiments were done using 50% by volume, 50 mM borate buffer at pH 8.6, and 50% 10 mM TE (10 mM Tris + 1 mM EDTA) TE buffer pH 8.0. Modified and bare gold nanoparticles have shown greater stability in sodium borate buffer than in the presence of other salts, such as sodium phosphate and sodium chloride. TE buffer was chosen because it is routinely used by molecular biologists when manipulating DNA.

4 Results and Discussion

Figure 2.8 shows the scattering signals for $30° \leq \theta \leq 150°$ for the Au–DNA hybridization with different concentrations of oligo-target. As the scattering intensity integrated across all angles increases with target concentrations, these results are consistent with literature results [116], where UV–vis measurements have shown that extinction increases as a function of target concentration.

Figure 2.9 further illustrates the sensitivity of the ADLS signal to the formation of Au–DNA aggregates using dissymmetry ratio analysis. Dissymmetry ratio analysis

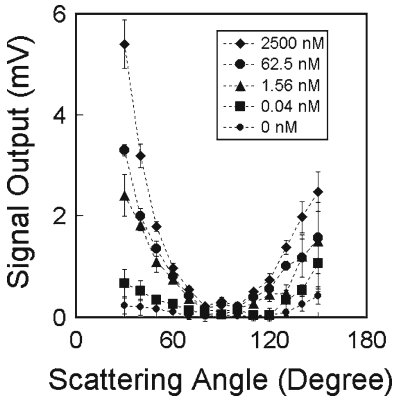

Fig. 2.8 Raw Au–DNA scattering data showing dependence on target concentration: 2,500 nM (*diamond*), 62.5 nM (*circle*), 1.56 nM (*triangle*), 0.04 nM (*square*), and no target oligonucleotide (*small circle*)

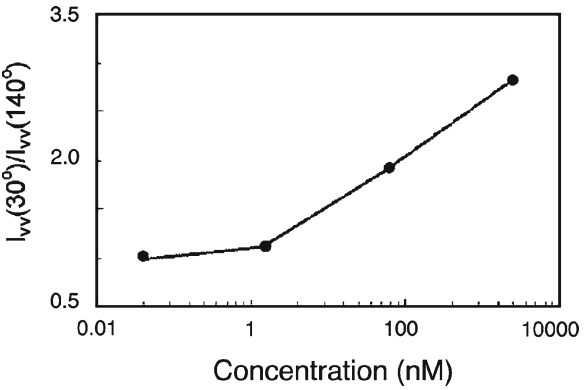

Fig. 2.9 Dissymmetry ratio analysis for raw data of Fig. 2.8

evaluates the ratio between the intensity of forward scattering at 30° and back scattering at 140°. Although this method does not provide quantitative information about the structure of Au–DNA aggregates, it can provide sensitivity to the concentration of the target DNA utilizing a simple instrumental configuration. The increase in the dissymmetry ratio as a function of target concentration results from the increase in volume of the Au–DNA aggregates. The lack of sensitivity at low concentrations of target DNA shown in these results suggests that the low target concentration measurements are near the detection limit of this approach.

Fractal dimension and Guinier analyses can provide quantitative structural information about the Au–DNA aggregates and can do so with greater sensitivity than the dissymmetry ratio analysis. Both Fractal Dimension Analysis (2.23) and Guinier Analysis (2.22) of the raw-scattering data shown in Fig. 2.8 is shown in Fig. 2.10. Numerical results for theses analyses are shown in Table 2.2. These results show that both the radius of gyration and the fractal dimension are found to be sensitive

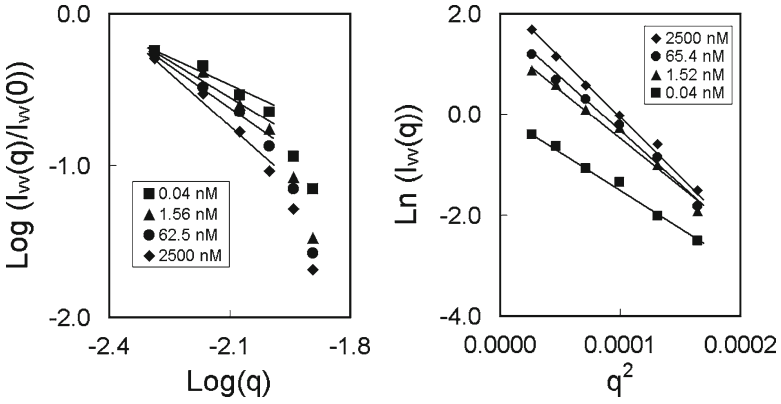

Fig. 2.10 Fractal and Guinier analyses for raw data of Fig. 2.8: 2,500 nM (*diamond*), 62.5 nM (*circle*), 1.56 nM (*triangle*), and 0.04 nM (*square*)

Table 2.2 R_g and Df as a function of oligonucleotide target concentration

Target concentration (nM)	R_g (nm)	Df
0.04	215	1.3
1.56	245	1.6
62.5	251	1.9
2,500	260	2.5

to target concentration. However, the latter shows a much greater sensitivity. As hypothesized, the increase in aggregate density (as shown by the increase in Df with oligo-target concentration) is likely the outcome of increased intraparticle cross-linking at higher oligo-target concentration.

The data of Fig. 2.10 suggest that the morphology of the aggregates can be measurably altered by target concentration. Figure 2.11 shows that the fractal dimension is also dependent on the length of the oligo-target, effectively increasing the spacing between the primary particles. To demonstrate this sensitivity, we compared the fractal dimension values for two systems with different oligo-target lengths: one in which the Au–DNA probe hybridizes to a 21-base long oligo-target, and the other in which the Au–DNA probe hybridizes to a 30-base long oligo-target. Each concentration of target showed lower Df values for the system containing the 30-base long oligo-target, in comparison to the one containing 21-base long oligo-target, indicative of more swollen and better solvated aggregates for the former. Further, the increase in fractal dimension with concentration for both lengths of oligo-target further suggests a transition from string-like aggregates (when Df is near unity) to denser, more compact structures at higher fractal dimension. This exponential dependence of the signal intensity on Df (2.2) makes this method very sensitive and therefore ideal for detecting an oligo-target DNA fragment using Au–DNA probes.

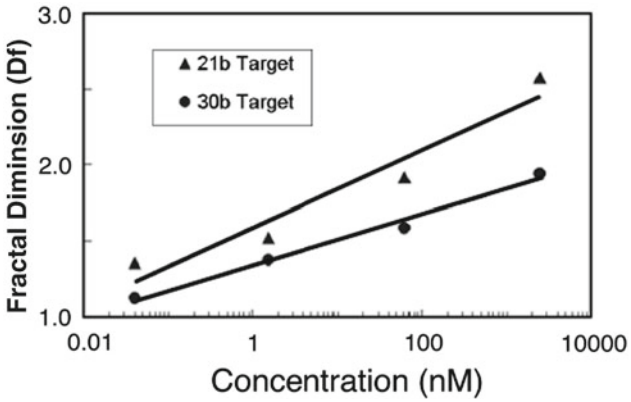

Fig. 2.11 Df as a function of concentration of 21 base- and 30 base-long target oligonucleotides

More quantitative information about the lengths of the targets can be extracted from the ratio between the slopes of the curves shown in Fig. 2.11. This can be accomplished by rewriting (2.21) as:

$$\mathrm{Df} = \frac{\log(N) - \log(kg)}{\log\left(\frac{R_g}{a}\right)} = \frac{\log(N)}{\log\left(\frac{R_g}{a}\right)} - \frac{\log(kg)}{\log\left(\frac{R_g}{a}\right)} \approx \frac{\log(C)}{\log\left(\frac{R_g}{a}\right)} - \frac{\log(kg)}{\log\left(\frac{R_g}{a}\right)}, \quad (2.24)$$

where C is the target concentration, where we assume that N and C are equivalent for this analysis. Then the slope of the curves in Fig. 2.11 is

$$\mathrm{Slope} = \frac{1}{\log\left(\frac{R_g}{a}\right)}. \quad (2.25)$$

Since a is the same for both systems, and if we assume that the two systems (21 bases and 30 bases) have the same number of particles forming an aggregate at each concentration and that the only difference between the two aggregates is the length between the targets, the ratio between the radii of gyrations should reflect the ratio between the length of the two linkers. This latter quantity can be estimated using molecular modeling software as 7.1 nm (21 bases) and 10.2 nm (30 bases). This ratio in lengths of 1.43 is slightly higher than the value extracted from the slopes, 1.26, but is within the uncertainty of the slope determinations.

5 Studies of Protein–Cofactor and Protein–Protein Interactions

In this section, we briefly describe several initial studies that demonstrate how the ADLS can be applied toward the detection and characterization of protein–cofactor and protein–protein interaction through the assembly of nanoparticle aggregates. The general approach for this methodology is to modify gold nanoparticles with a ligand moiety, a cofactor or a protein, that specifically interacts with a target protein, where the interaction induces the assembly of the Au–protein aggregate.

5.1 The Streptavidin–Biotin Complex

An example of a ligand protein system is the streptavidin–biotin complex. Streptavidin is a four-unit 50 kDa recombinant protein [117] that has four binding sites. Biotin (vitamin H) tightly binds to streptavidin with a dissociation constant of 10^{-15} M. The streptavidin–biotin complex has been extensively described in the literature [117–122]. Both biotin and streptavidin can be chemically modified with sulfide (or disulfide) containing linkers and/or other cross-linkers. Finally, the size, shape, and position of binding sites in the protein can be varied by means of a simple one-step conjugation chemistry using a homobifunctional cross-linker (glutaraldehyde) [123, 124] that allows streptavidin to be cross-linked to itself, forming dimers, trimers, and larger protein complexes.

The strong binding between the protein and cofactor occurs through noncovalent interactions consisting of hydrogen bonding between biotin and the serine (Ser) and aspartate (Asp) residues in the streptavidin binding site, and hydrophobic interaction between the biotin tail and the streptavidin side chains along the binding site [118, 119, 125]. Our anticipation was that the interaction through the four available binding sites would allow streptavidin to be used as a cross-linker between biotin-modified gold nanoparticles forming a fractal assembly, as illustrated in Fig. 2.12.

5.1.1 Thiol–Biotin Conjugation

The approach taken to functionalize the Au nanoparticles was to use disulfide moiety to anchor biotin to the surface of the Au nanoparticles. The first step was to chemically modify biotin with L-cystine (cystine), a disulfide-containing molecule. Cystine is an amino acid derived from two cysteine bridged through a disulfide bond. The choice of using the disulfide form instead of plain cysteine or another amine-thiol containing molecule, such as meracaptoethalamine, was because it has been reported that gold SAM originated from di-*n*-alkyl disulfides (RSSR) are more stable than those from alkanethiols (RSH) [99, 103, 104, 109, 110].

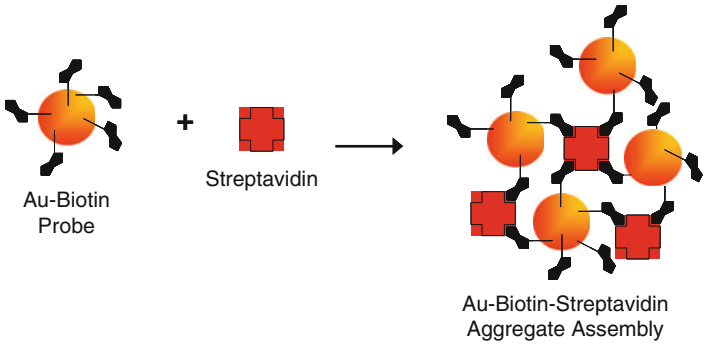

Fig. 2.12 Illustration of cofactor modified biotin (Au-ligand probe) interacting with a target protein to form an Au–protein aggregate

The coupling chemistry used NHS ester modified biotin to generate the disulfide modified biotin. NHS ester cross-linkers are routinely used for modifying proteins and protein cofactors, such as biotin. The NHS ester group reacts with the deprotonated form of the primary amine by nucleophilic attack, which forms a stable amide linkage and *N*-hydroxysuccinimide is released as the by-product of the reaction [124, 126]. Hydrolysis of the NHS ester is a major competing reaction in aqueous solution, and the rate of hydrolysis increases with increasing pH.

5.1.2 Gold–Biotin Coupling

The covalent linkage between the Au nanoparticle and the disulfide-modified biotin (L-cystine-biotin or cyss-biotin) was done through the disulfide bond of the cystine and the Au nanoparticle. The preferred mechanism, which has been supported by experimental data and theoretical calculations [103–109], is the one where the disulfide bond is broken close to the surface with the generation of two thiolates (RS^-) which then adsorbs onto Au [110]:

$$R-S-S-R+Au_n^0 \rightarrow R-S^-Au^+\cdot Au_n^0$$

Existing literature shows that the rates of adsorption of *n*-alkyl-disulfides is indistinguishable from alkanethiols, but the rate of replacement for thiols is much faster than for disulfides [103, 110, 127]. It also has been suggested that the estimated adsoption energy for dialkyl disulfides is twice as favorable as the adsorption energy for thiols [110, 128]. Determining the exact mechanism of adsorption of thiols and disulfides on gold nanoparticles is not an easy task [103], which explains different opinions on the exact mechanism of thiol and disulfide chemisorption on gold [99, 100, 104, 110]. The theoretical coverage of a SAM on Au is approximately 0.77 nmol/cm^2 [99].

Usually, Au nanoparticles carry an overall negative charge resulting from either citrate groups present on its surfaces resulting from the citrate reduction process during its synthesis, or from hydroxy and chloride groups present in solution which weakly adsorb onto Au nanoparticles [99]. When a thiol or disulfide-containing molecule adsorbs onto the surface of an Au nanoparticle, the overall surface charge of the Au nanoparticle changes. This charge displacement can induce an aggregation of the Au nanopartilcles which can be detected by monitoring the red shift in the plasmon resonance absorption wavelength when aggregation takes place [99, 100, 116].

We determined that cystine concentrations higher than 1.56 mM induce aggregation of 40 nm Au, but that concentrations as high as 12.5 mM cystine do not induce aggregation of 100 nm Au nanoparticles. We also tested the behavior of unmodified particles in the presence of cystine-modified biotin (cys-biotin). In contrast to the cystine experiment, the highest concentration of cyss-biotin available in our stock solution was 0.450 mM, which is approximately three times lower than the cystine concentration that induced aggregation. Both sizes of Au nanoparticles showed negligible aggregation. Unbound cys-biotin was removed through four sequential centrifugation steps (at 14,000 rpm for 15 min), where the supernatant was removed and the sedimented Au is resuspended with nanopure water.

5.1.3 Scattering Signal as a Function of Streptavidin-Complex Concentration

Figure 2.13 shows the angle-resolved scattering signal as a function of streptavidin-complex (target) concentration. The sensitivity of the scattering signal to the concentration of the streptavidin-complex is especially pronounced at forward-scattering angles. Also shown is a control experiment in which unmodified biotin was added to the streptavidn mixture before adding the Au-Biotin probes. The fractal dimension and Guinier analysis for these same experiments are shown in Fig. 2.14. These results indicate that both the radius of gyration and the fractal dimension are sensitive to target streptavidin-complex concentration. However, the latter shows a greater sensitivity. These results also show that the control sample (streptavidin saturated with unmodified biotin) remains nearly unchanged for the various concentrations of protein.

5.1.4 Fractal Dimension Comparison of Streptavidin Monomer and Complex as Target Protein

In this study, we compared the difference in fractal dimensions in aggregates assembled with either streptavidin-complexes or with streptavidin monomers as the protein target. Both 532 and 632 nm excitation light were used, with very similar results. The results of the Guinier and Fractal Dimension Analyses for this system, shown in Fig. 2.14, suggest that the morphology of the aggregates is a function of protein concentration, but also the structure of the target protein. The mixture of larger protein targets, which make up the streptavidin-complex, assembles the Au

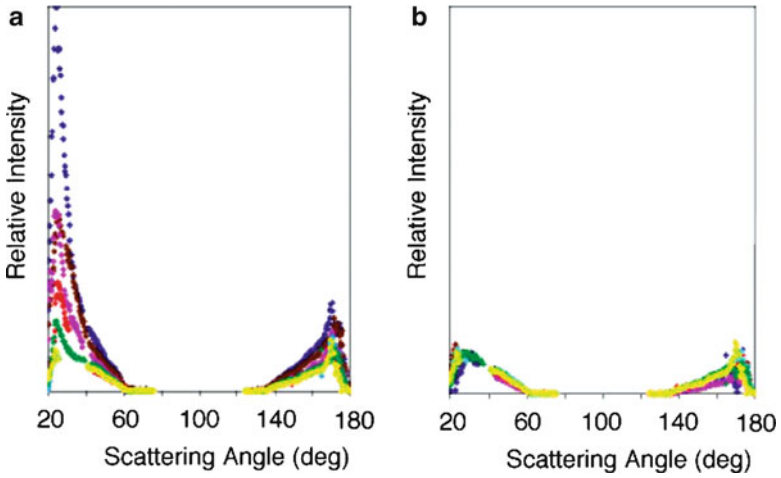

Fig. 2.13 (**a**) Angle-resolved scattering signal for 40 nm Au-biotin probes incubated with various concentrations of streptavidin complexes: 50 nM (*purple*), 25 nM (*brown*), 12.5 nM (*pink*), 6.25 nM (*red*), 3.12 nM (*green*), and no streptavidin (*yellow*; control). (**b**) Control where the streptavidin-complex binding sites from (**a**) were blocked with free biotin (100 μM) prior to mixing with Au-biotin probes. Higher complex concentration showed increase scattering signal (*arrow*)

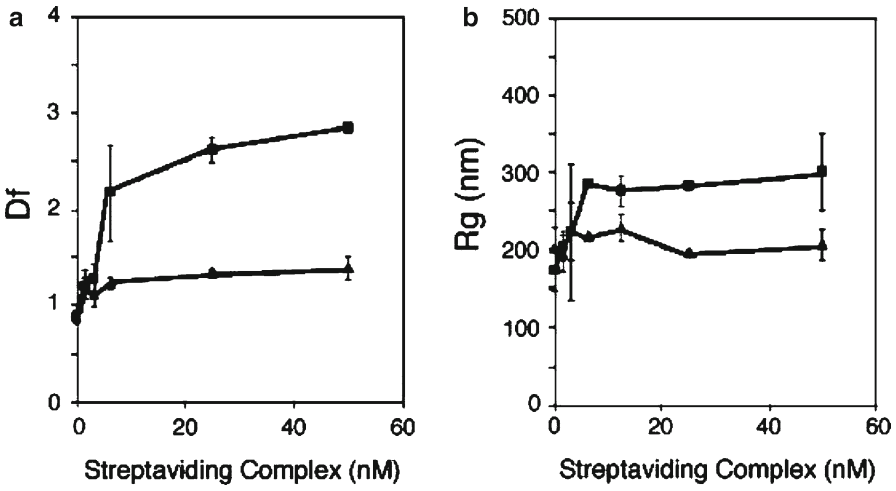

Fig. 2.14 Df of 40 nm Au-biotin as a function of streptavidin complex aggregate (*square*); and R_g of 40 nm Au-biotin as a function of streptavidin complex aggregate (*square*). Control (*triangle*) consists of streptavidin complexes saturated with unmodified biotin prior to introducing Au-biotin

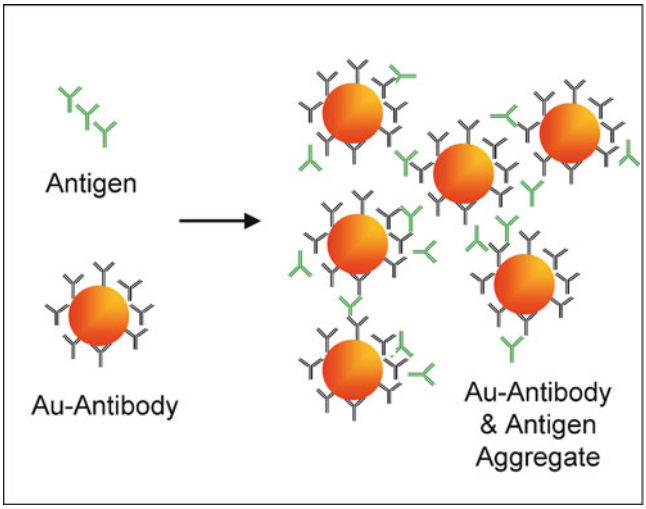

Fig. 2.15 Illustration of antigen-induced aggregation of antibody modified Au nanoparticles (Au-antibody)

nanoparticles into less dense (but probably better solvated) aggregates. However, both systems show an increase in fractal dimension with added protein concentrations, analogous to the behavior observed using the Au–DNA probes.

5.2 Antigen Detection Using Antibody-Modified Au Nanoparticles

To demonstrate an application in an even more complex system, a protein–protein binding event, we applied ADLS and fractal dimension to detect the reaction of 40-nm Au nanoparticles modified with goat antibodies toward a target antigen. The Au nanoparticles were modified with either goat anti-mouse immunoglobulin (Gt anti-Ms IgG) or goat anti-human immunoglobulin (Gt anti-Hu IgG); the target antigen was mouse immunoglobulin G protein (Mouse IgG), which should be reactive mainly with Gt anti-Ms IgG on gold nanoparitcle, as illustrated in Fig. 2.15.

Since an IgG has two binding sites available to interact with an antigen, we anticipated that the presence of a target antigen would trigger the aggregation of the antibody-modified Au nanoparticles, forming an aggregate of nanoparitcle, antibody, and antigen. The results were in agreement with these predictions. Figure 2.16 shows the forward-scattering signal for the two antibody systems and a control. Table 2.3 shows fractal dimensions for the three systems. A system consisting of nanoparticles carrying the Gt anti-Ms IgG antibody showed the highest reactivity toward the target mouse IgG antigen as reflected in the greater forward scattering

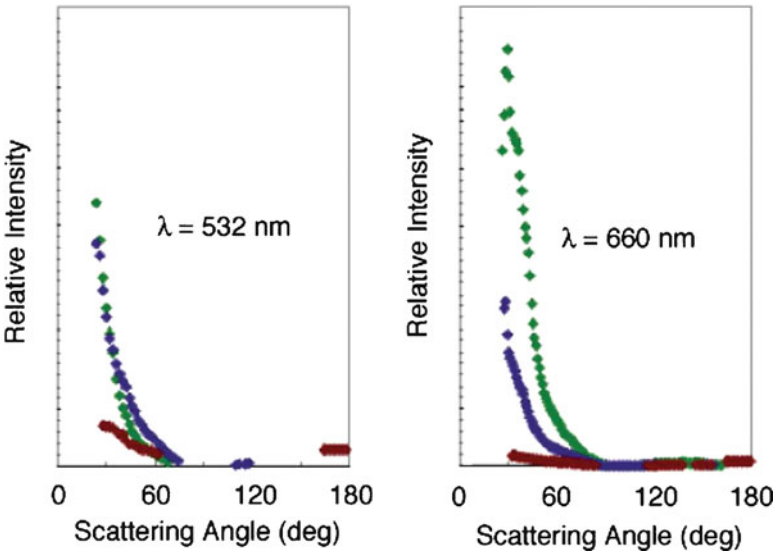

Fig. 2.16 ADLS measurements using 532 nm (*left*) and 660 nm (*right*) incident laser light. Au-anti-Ms IgG (*triangle*), Au-anti-Hu IgG (*square*), and control (Au-anti-Ms IgG; *circle*)

Table 2.3 Df of Au-antibody–antigen aggregates

	Df λ_{ext} = 532 nm	Df λ_{ext} = 660 nm
Au–Gt anti-Ms IgG	2.86 ± 0.05	2.95 ± 0.20
Au–Gt anti-Hu IgG	2.40 ± 0.05	2.32 ± 0.07
Control, Au–Gt anti-Ms IgG	1.65 ± 0.10	1.87 ± 0.03

and the greatest fractal dimension. However, the system in which Au nanoparticles were modified with Gt anti-Hu also showed an increased forward-scattering signal, which indicates cross reactivity between the Gt anti-Hu IgG antibody toward mouse IgG. This is not a surprising result because the Gt anit-Hu bound to the Au nanoparticles are not "mouse serum adsorbed" grade, which means that the Gt anti-Hu IgG which cross react with mouse IgG were not removed during the affinity purification process. Further, because of the common mammalian denomination of humans and mouse, Gt anti-Hu antibodies still show cross reactivity to mouse IgG, as our results suggest.

The use of Au nanoparticles and fractal dimension analysis could be further adapted toward the determination of antibody titer toward a specific antigen. Because antibodies are being routinely developed to be used in drug discovery as drug delivery and diagnostic agents, the determination of the reactivity with target antigen must be accompanied by measurement of its cross reactivity with other proteins. This experiment is a good example, where the Au nanoparticles modified with Gt anti-Hu showed cross reactivity toward the mouse IgG.

6 Future Trends and Possibilities

This chapter presents an innovative approach where ADLS-FA can be used to probe biomolecular assembly processes. Probing these events in a protein's or nucleic acid's native environment is an important step toward the eventual use of biopolymer modified nanoparticles as building blocks for nanostructure assembly. The method provides the flexibility for defining different biosensor formats, by using either the assembly of Au-biopolymer aggregates or the disassembly of these aggregates as the signal transducers. For example (and in contrast to the aggregate assembly demonstrated here), one could take advantage of aggregate disassembly by creating nanoparticle-biopolymer aggregates, where the protein or nucleic acid bridging the nanoparticles undergoes translocation upon contact with a specific protein or molecule. As a result of this translocation or cleaving, the disassembly and/or change in fractal dimension of these aggregates takes place. Many enzymatic-mediated processes are accompanied by translocation, such as, proteolytic digestion of protein by proteases, DNA and RNA cleavage by restriction enzymes and many phosphorylation-mediated processes.

Another direction we are pursuing is the combination of ADLS/FD with inelastic scattering, specially surface-enhanced Raman scattering (SERS), to attempt to extract not only structural information about the Au-biopolymers through ADLS/FD, but also to obtain information about chemical interaction between the biopolymer and Au-probe at the interface between particle and solution. This could be particularly useful for studying peptide–protein interactions, where Au nanoparticles are modified with peptides. There is also considerable interest in understanding the process of SERS, and increased attention has been paid in the relationship between the large surface enhancements and fractal dimension characteristics of metal surfaces and metal nanoparticle assemblies.

References

1. Souza, G.R. and J.H. Miller, *Oligonucleotide detection using angle-dependent light scattering and fractal dimension analysis of gold-DNA aggregates.* Journal of the American Chemical Society, 2001. **123**(27): p. 6734–6735.
2. Souza, G.R. and J.H. Miller, *Fractal Dimension Analysis Of Nanoparticle Aggregates Using Angle Dependent Light Scattering For The Detection And Characterization Of Nucleic Acids And Proteins.* 2003: USPTO Application.
3. Farias, T.L., U.O. Koylu, and M.G. Carvalho, *Range of validity of the Rayleigh-Debye-Gan theory for optics of fractal aggregates.* Appl. Opt., 1996. **35**(33): p. 6560.
4. Johnson, C.P., X. Li, and B.E. Logan, Env. Sci. & Tech., 1996. **30**: p. 1911.
5. Bushell, G.C., R. Amal, and J.A. Raper, *The effect of a bimodal primary particle size distribution on scattering from hematite aggregates.* Physica A: Statistical and Theoretical Physics, 1996. **233**(3–4): p. 859–866.
6. Thill, A., et al., *Structural Interpretations of Static Light Scattering Patterns of Fractal Aggregates; II. Experimental Study.* Journal of Colloid and Interface Science, 2000. **228**(2): p. 386–392.

7. Zenkevich, A.V., et al., *Formation of Au fractal nanoclusters during pulsed laser deposition on highly oriented pyrolitic graphite.* Physical Review B, 2002(65).
8. Forrest, S.R. and T.A. Witten, J. Phys. A, 1979. **12**: p. L109.
9. Schaefer, D.W., et al., *Fractal Geometry of Colloidal Aggregates.* Phys. Rev. Lett., 1984. **52**: p. 2371–2374.
10. Weitz, D.A. and M. Oliveria, *Fractal Structures formed by Kinetic Aggregation of Aqueous Gold Colloids.* Phys. Rev. Lett., 1984. **52**: p. 1433–1436.
11. Weitz, D.A., et al., Phys. Rev. Lett., 1984. **53**: p. 1657.
12. Weitz, D.A., et al., *Limits of the Fractal Dimension for Irreversible Kinetic Aggregation of Gold Colloids.* Phys. Rev. Lett., 1985. **54**(13): p. 1416–1419.
13. Schaefer, D.W. and K.D. Keefer, Phys. Rev. Lett., 1986. **56**: p. 2199.
14. Chen, S.H. and J. Teixeira, Phys. Rev. Lett., 1986. **57**: p. 2583.
15. Aubert, C. and D.S. Cannell, Phys. Rev. Lett., 1986. **56**: p. 738–740.
16. Dimon, P., et al., Phys. Rev. Lett., 1986. **57**: p. 595.
17. Wong, K., B. Cabane, and R.J. Duplessix, J. Colloid and Interface Sci., 1988. **123**: p. 466.
18. Hurd, A.J. and W.L. Flower, J. Colloid and Interface Sci., 1988. **122**: p. 178.
19. Wilcoxon, J.P., J.E. Martin, and D.W. Schaefer, *Aggregation in colloidal gold.* Phys. Rev. A, 1989. **39**: p. 2675–2688.
20. Martin, J.E., et al., Phys. Rev. A, 1990. **41**: p. 4379.
21. Olivier, B.J. and C.M. Sorensen, *Variable aggregation rates in colloidal gold: Kernel homogeneity dependence on aggregant concentration.* Phys. Rev. A, 1990. **41**: p. 2093–2100.
22. Amal, R., et al., *Structure and kinetics of aggregating colloidal haematite.* Colloids and Surfaces, 1990. **46**(1): p. 1–19.
23. Liu, J., et al., *Fractal colloidal aggregates with finite interparticle interactions: Energy dependence of the fractal dimension.* Physical Review A, 1990. **41**(6): p. 3206–3213.
24. Stoll, S., A. Elaissari, and E. Pefferkorn, J. Colloid and Interface Sci., 1990. **140**: p. 98.
25. Schaefer, D.W., et al., Aerosol Sci., 1991. **22**: p. S447.
26. Foret, M., J. Pelous, and R. Vacher, J. de Physique, 1992. **2**: p. 791.
27. Sorensen, C.M., J. Cai, and N. Lu, Appl. Opt., 1992. **31**(30): p. 6547–6557.
28. Oles, V., J. Colloid and Interface Sci., 1992. **154**: p. 351.
29. Cai, J., N. Lu, and C.M. Sorensen, Langmuir, 1993. **9**: p. 2861.
30. Stankiewicz, J., et al., Progr. Colloid & Polymer Sci., 1993. **93**: p. 358.
31. Carpineti, M. and M. Giglio, Adv. Colloid and Interface Sci., 1993. **46**: p. 73.
32. Amal, R., D. Gazeau, and T.D. Waite, Part. & Part. Syst.Charact. II, 1994: p. 315–320.
33. Weber, A.P., J.D. Thorne, and S.K. Friedlander, MRS Symposium Proceedings, 1995. **380**: p. 87.
34. Lin, M.Y., et al., Nature, 1989. **339**: p. 360.
35. Lin, J., et al., *Gold-Coated Iron (Fe@Au) Nanoparticles: Synthesis, Characterization, and Magnetic Field-Induced Self-Assembly.* Journal of Solid State Chemistry, 2001. **159**(1): p. 26–31.
36. Burns, J.L., et al., Langmuir, 1997. **13**: p. 6413–6420.
37. McCauley, J.L., *Chaos, Dynamics, and Fractals*. 1994: Cambridge University Press.
38. Avnir, D., D. Farin, and P. Pfeifer, *Chemistry in noninteger dimensions between two and three. II. Fractal surfaces of adsorbents.* J. Chem. Phys., 1983. **79**(7): p. 3566–3569.
39. Avnir, D. and P. Pfeifer, *Fractal Dimension in Chemistry. An Intensive Characteristic of Surface Irregularity.* Nouveau Journal De Chimie, 1983. **7**(2): p. 71–73.
40. Avnir, D., D. Farin, and P. Pfeifer, Nature, 1984. **308**: p. 261–263.
41. Koylu, U.O. and G.M. Faeth, *Optical Properties of Overfire Soot in Buoyant Turbulent Diffusion Flames at Long Residence Times.* Transactions of the ASME, 1994. **116**: p. 152–159.
42. Sorensen, C.M., N. Lu, and J. Cai, *Fractal Cluster Size Distribution Measurement Using Static Light Scattering.* Journal of Colloid and Interface Science, 1995. **174**(2): p. 456–460.
43. Sorensen, C.M., et al., *Aerogelation in a Flame Soot Aerosol.* Physical Review Letters, 1998. **80**(8): p. 1782.

44. Sorensen, C.M. and C. Oh, *Divine proportion shape preservation and the fractal nature of clster-cluster aggregates.* Physical Review E, 1998. **58**(6): p. 7545.
45. Sorensen, C.M. and G.M. Wang, *Size distribution effect on the power law regime of the structure factor of fractal aggregates.* Physical Review E, 1999. **60**(6): p. 7143.
46. Bushell, G.C., et al., *On techniques for the measurement of the mass fractal dimension of aggregates.* Advances in Colloid and Interface Science, 2002. **95**(1): p. 1–50.
47. Bonczyk, P.A. and R.J. Hall, Langmuir, 1991. **7**: p. 1274–1280.
48. Dewey, T.G., *Fractal in Molecular Biophysics*. 1997, New York: Oxford University Press.
49. Mandelbrot, B.B., *The Fractal Geometry of Nature*. 1982, San Francisco: Freeman.
50. Mandelbrot, B.B., *Les Objets Fractals: Forme, Hasard et Dimension.* 1975, Paris: Flammarion.
51. Schroeder, M., *Fractals, Chaos, and Power Laws*. 1991, New York: W. H. Freeman and Company.
52. van de Hulst, H.C., *Light Scattering by Small Particles*. 1981, New York: Dover.
53. Young, A.T., Physics Today, 1982. **35**(1): p. 42–48.
54. Muller, R.H. and W. Mehnert, *Particle and Surface Characterisation Methods*. 1997: GmbH Scientific Publishers.
55. Bohren, C.F. and D.R. Huffman, *Absorption and Scattering of Light by Small Particles*, ed. D.R. Huffman. 1983, New York: John Wiley and Sons, Inc.
56. Sorensen, C.M., *Scattering and Absorption of Light by Particles and Aggregates*, in *Handbook of Surface and Colloid Chemistry*, K.S. Birdi, Editor. 1997, CRC Press: New York.
57. Kerker, M., *The Scattering of Light and other Electromagnetic Radiation*. 1969, New York: Academic Press.
58. Berne, B. and R. Pecora, *Dynamic light scattering: with applications to chemistry, biology, and physics*. 2nd Edition ed. 2000, New York: Dover.
59. Saleh, B.E. and M.C. Teich, *Fundamentals of Photonics*. 1991, New York: Wiley, John & Sons, Inc.
60. Hunter, R.J., *Introduction to Modern Colloid Science*. 1993, New York: Oxford Science Publications.
61. Gillilanda, K.O., et al., *Distribution, spherical structure and predicted Mie scattering of multilamellar bodies in human age-related nuclear cataracts.* Experimental Eye Research, 2004. **79**: p. 563–576.
62. Mountain, R.D. and G.W. Mulholland, Langmuir, 1998. **4**: p. 1321–1326.
63. Avnir, D. and P.W. Schmidt, *The Fractal Approach to Heterogeneous Chemistry.*, ed. D. Avnir. 1989, New York: John Wiley & Sons, Inc.
64. Pfeifer, P. and D. Avnir, *Chemistry in noninteger dimensions between two and three. I. Fractal theory of heterogeneous surfaces.* J. Chem. Phys., 1983. **79**(7): p. 3558.
65. Kimura, H., *Light-scattering properties of fractal aggregates: numerical calculations by a superposition technique and the discrete-dipole approximation.* Journal of Quantitative Spectroscopy and Radiative Transfer, 2001. **70**(4–6): p. 581–594.
66. Lambert, S., et al., *Structural Interpretations of Static Light Scattering Patterns of Fractal Aggregates; I. Introduction of a Mean Optical Index: Numerical Simulations.* Journal of Colloid and Interface Science, 2000. **228**(2): p. 379–385.
67. Wang, G. and C.M. Sorensen, *Experimental test of the Rayleigh-Debye-Gans theory for light scattering by fractal aggregates.* Applied Optics, 2002. **41**(22): p. 4645–4651.
68. Castellano, A.C., et al., *X-ray small angle scattering of the human transferrin protein aggregates. A fractal study.* Biophysical Journal, 1993. **64**(2): p. 520–524.
69. Seri-Levy, A. and D. Avnir, *Fractal analysis of surface geometry effects on catalytic reactions.* Surface Science, 1991. **248**(1–2): p. 258–270.
70. Pfeifer, P., D. Avnir, and D. Farin, *Ideally irregular surfaces, of dimension greater than two, in theory and practice.* Surface Science, 1983. **126**(1–3): p. 569–572.
71. Shalaev, V.M., M.I. Stockman, and R. Botet, *Resonant excitations and nonlinear optics of fractals.* Physica A: Statistical and Theoretical Physics, 1992. **185**(1–4): p. 181–186.

72. Danilova, Y.E., A.I. Plekhanov, and V.P. Safonov, *Experimental study of polarization-selective holes, burning in absorption spectra of metal fractal clusters.* Physica A: Statistical and Theoretical Physics, 1992. **185**(1–4): p. 61–65.
73. Carl, A., G. Dumpich, and S. Friedrichowski, *Electron diffusion in percolating gold clusters.* Physica A: Statistical and Theoretical Physics, 1992. **191**(1–4): p. 454–457.
74. Koylu, U.O. and G.M. Faeth, Transactions of the ASME, 1994. **116**: p. 971–979.
75. Farias, T.L., U.O. Koylu, and M.G. Carvalho, *Effects of polydispersity of primary particle and aggregate sizes on radiative properties of simulated soot.* J. Quant. Spectrosc. Radiat. Transfer, 1995. **55**: p. 357–371.
76. Bushell, G.C., *Primary particle polydispersity in fractal aggregates*, in *Chemical Enginnering and Industrial Chemistry*. 1998, New South Wales: New South Wales. p. 202.
77. Marsh, P., G. Bushell, and R. Amal, *Scattering Behavior of Restructured Aggregates: A Simulation Study.* Journal of Colloid and Interface Science, 2001. **241**(1): p. 286–288.
78. Selomulya, C., et al., *Evidence of Shear Rate Dependence on Restructuring and Breakup of Latex Aggregates.* Journal of Colloid and Interface Science, 2001. **236**(1): p. 67–77.
79. Khlebtsov, N.G. and A.G. Melnikov, *Structure Factor and Exponent of Scattering by Polydisperse Fractal Colloidal Aggregates.* Journal of Colloid and Interface Science, 1994. **163**(1): p. 145–151.
80. Harding, S.E., D.B. Sattelle, and V.A. Bloomfield, *Laser Light Scattering in Biochemistry*, ed. V.A. Bloomfield. 1992, England: Redwood Press Ltd.
81. Stover, J.C. Optical Scattering Measurements and Analysis. 1995, Bellingham: The Society for Optical Engineering.
82. Yguerabide, J. and E.E. Yguerabide, Anal. Biochemistry, 1998. **262**: p. 137–156.
83. Parkash, J., et al., Biophysical Journal, 1998. **74**: p. 2089–2099.
84. Trulson, M.O., et al., SPIE, 1998. **3259**: p. 234–240.
85. Bryant, G. and J.C. Thomas, Langmuir, 1995. **11**: p. 2480–2485.
86. Gabriel, M.K. and E.T. McGuinness, FEBS Letters, 1984. **175**(2): p. 419–421.
87. Korgel, B.A., J.H. Van Zanten, and H.G. Monbouquette, Biophysical Journal, 1998. **74**: p. 3264–3272.
88. Machtle, W., Biophysical Journal, 1999. **76**: p. 1080–1091.
89. Qian, R.L., R. Mhatre, and I.S. Krull, J. of Chromatography, 1997. **787**: p. 101–109.
90. Tsutsui, K., K. Koya, and T. Kato, *An investigation of continuous-angle laser light scattering.* Review of Scientific Instruments, 1998. **69**(10): p. 3482.
91. Chu, B., *Laser Light Scattering*. 1974, New York: Academic Press.
92. Mujumdar, S.R., et al., Bioconjugate Chem., 1996. **7**: p. 356–362.
93. Pow, D.V. and J.F. Morris, *Membrane routing during exocytosis and endocytosis in neuroendocrine neurons and endocrine cells: Use of colloidal gold particles and immunocytochemical discrimination of membrane compartments.* Cell Tissue Res., 1991. **264**: p. 299–316.
94. Horisberger, M., *Evaluation of colloidal gold as a cytochemical marker for transmission and scanning electron microscope.* Biol. Cell, 1979. **36**: p. 253–258.
95. Horisberger, M. and M.F. Celerc, *Labeling of golloidal gold with protien A.* Histochemistry, 1985. **82**: p. 219.
96. Horisberger, M. and J. Rosset, *Colloidal gold, a useful marker fo transmission and scanning electron microscopy.* J. Histochem. Cytochem., 1977. **25**: p. 295.
97. Horisberger, M., J. Rosset, and H. Bauer, *Colloidal gold granules as markers for cell surface receptors in the scanning electron microscope.* Experientia, 1975. **31**: p. 1147–1149.
98. Horisberger, M. and M. Tacchini-Vonlanthen, *Ultrastructural localization of Kunitz inhibitor on thin sections of Glcine max (soybean) cv. Maple Arrow by the gold method.* Histochemistry, 1983. **77**: p. 37–50.
99. Weisbecker, C.S., M.V. Merritt, and G.M. Whitesides, *Molecular Self-Assembly of Aliphatic Thiols on Gold Colloid.* Langmuir, 1996. **12**(16): p. 3763–3772.
100. Whitesides, G.M., et al., Critical Reviews in Surface Chemistry, 1993. **3**(1): p. 49–65.
101. Bamdad, C., Biophysical Journal, 1998. **75**: p. 1997–2003.

102. Bryant, M.A. and J.E. Pemberton, J. Am. Chem. Soc., 1991. **113**: p. 8284–8293.
103. Gronbeck, H., A. Curioni, and W. Andreoni, *Thiols and Disulfides on the Au(111) Surface: The Headgroup-Gold Interaction.* J. Am. Chem. Soc., 2000. **122**: p. 3839–3842.
104. Ulman, A., et al., *Mixed alkanethiol monolayers on gold surfaces: Wetting and stability studies.* Advances in Colloid and Interface Science, 1992. **39**: p. 175–224.
105. Walczak, M.W., et al., J. Am. Chem. Soc., 1991. **113**: p. 2370.
106. Porter, M.D., et al., J. Am. Chem. Soc., 1987. **109**: p. 3559.
107. Nuzzo, R.G., F.A. Fusco, and D.L. Allara, J. Am. Chem. Soc. **109**: p. 2358.
108. Bain, C.D., H.A. Biebuyck, and G.M. Whitesides, Langmuir, 1989(5): p. 723.
109. Nuzzo, R.G., B.R. Zegarski, and L.H. Dubois, J. Am. Chem. Soc., 1987(109): p. 733.
110. Ulman, A., *Formation and Structure of Self-Assembled Monolayers.* Chem. Rev., 1996. **96**: p. 1533–1554.
111. Herne, T.M. and M.J. Tarlov, J. Am. Chem. Soc., 1998. **119**: p. 8916–8920.
112. Elghanian, R., et al., Science, 1997. **227**(5329): p. 1078–1081.
113. Storhoff, J.J. and C.A. Mirkin, Chem. Rev, 1999. **99**: p. 1849–1862.
114. Lewis, M. and M.J. Tarlov, J. Am. Chem. SOc., 1995. **117**: p. 9574–9575.
115. Peterlinz, K.A., et al., J. Am. Chem. Soc., 1997. **119**: p. 3401–3402.
116. Reynolds, R.A., C.A. Mirkin, and R.L. Letsinger, J. Am. Chem. Soc., 2000. **122**: p. 3795–3796.
117. Savage, D., G. Mattson, and S. Desai, *Avidin-Biotin Chemistry: A Handbook*. 1992, Rockford, IL.: Pierce Chemical.
118. Katz, B., B. Liu, and R. Cass, *Structure-Based Design Tools: Structural and Thermodynamic Comparison with Biotin of a Small Molecule That Binds to Streptavidin with Micromolar Affinity.* J. Am. Chem. Soc., 1996. **118**(34): p. 7914–7920.
119. Hyre, D.E., *Ser45 plays an important role in managing both the equilibrium and transition state energetics of the streptavidin-biotin system.* Protein Science, 2000. **9**: p. 878–885.
120. Badia, A., et al., *Probing the electrochemical deposition and/or desorption of self-assembled and electropolymerizable organic thin films by surface plasmon spectroscopy and atomic force microscopy.* Sensors and Actuators B: Chemical, 1999. **54**(1–2): p. 145–165.
121. Piscevic, D., W. Knoll, and M.J. Tarlov, *Surface plasmon microscopy of biotin-streptavidin binding reactions on UV-photopatterned alkanethiol self-assembled monolayers.* Supramolecular Science, 1995. **2**(2): p. 99–106.
122. Wang, J., et al., *Metal nanoparticle-based electrochemical stripping potentiometric detection of DNA hybridization.* Analytical Chemistry, 2001. **73**(22): p. 5576–5581.
123. Avrameas, S.a.T., T., *The cross-linking of proteins with glutaraldehyde and its use for the preparation of immunosorbents.* Immunochemistry, 1969. **6**: p. 53–66.
124. Wong, S.S. Chemistry of Protein Conjugation and Cross-Linking. 1993: CRC Press.
125. Freitag, S., et al., *Structural studies of the streptavidin binding loop.* Protein Science., 1997. **6**: p. 1157–1166.
126. Hermanson, G.T., *Bioconjugate Techniques*. 1996, San Diego: Academic Press.
127. Biebuyck, H.A. and G.M. Whitesides, Langmuir, 1994. **10**: p. 1825.
128. Schlenoff, j.B., M. Li, and H. Ly, J. Am. Chem. Soc., 1995. **117**: p. 12528.

http://www.springer.com/978-1-4614-0883-3

Reviews in Plasmonics 2010
Geddes, C.D. (Ed.)
2012, VIII, 334 p., Hardcover
ISBN: 978-1-4614-0883-3